Electronic Supplementary Information

Highly efficient electrooxidation of biomass-based 5-hydroxymethylfurfural to 2,5-furandicarboxylic acid over Cu-Ni bimetal-phytic acid hybrid electrocatalyst

Haishan Xu,[a] Yinghua Li,[a] Zhenbing Xie,*[b] Xin Wang,[c] Runlu Yang,[c] Haoran Wu*[c] and Yiyong Mai*[a]

[a]School of Chemistry and Chemical Engineering, Frontiers Science Center for Transformative Molecules, Shanghai Key Laboratory of Electrical Insulation and Thermal Ageing, Shanghai Jiao Tong University, Shanghai 200240, China.

[b]Department of Chemistry, Tangshan Normal University, Tangshan 063000, China.

[c]School of Chemical Engineering, Zhengzhou University, Zhengzhou 450001, China.

*Corresponding author E-mail: xzbing@tstc.edu.cn; haoranwu@zzu.edu.cn; mai@sjtu.edu.cn

1. Experimental section

Materials. Phytic acid solution (70%) was supplied by Sinophar Chemical Reagent Co., Ltd. Nickel acetate and copper acetate were purchased from Sinopharm Chemical Reagent. HMF, FDCA, 5-hydroxymethyl-2-furancarboxylic acid (HMFCA), and diformylfuran (DFF) were obtained from Aladdin Industrial Corporation. Amino tri(methylene phosphonic acid (ATMP, 50 wt% in water) was purchased from Tokyo Chemical Industry Co., Ltd. Nafion N-117 membrane, Nafion D-521 dispersion, and Toray Carbon Paper were supplied by Alfa Aesar China Co., Ltd. All chemicals were analytical grade and used without further purification.

Preparation of electrocatalysts. The electrocatalyst materials were prepared by a co-precipitation method. Taking Cu-Ni(1)@PA as an example, copper acetate (1.5 mmol) and nickel acetate (1.5 mmol) were dissolved in H_2O (75 mL) to form a homogeneous solution. Then, PA solution (0.25 mL) was added into the mixture stirring for 24 h at room temperature. After reaction, the blue solid was separated and washed with H_2O and ethanol, then was moved into the oven at 80 $^{\circ}C$ under vacuum for 24 h. Finally, the resultant solid was denoted as Cu-Ni(1)@PA. Similarly, other materials with different mole ratio of copper acetate and nickel acetate (e.g., 2:1 and 0.5:1) were also synthesized according to this method. In addition, other materials with different ligands (ATMP and BTC) were synthesized using a similar route, and named by Cu-Ni(2)@ATMP and Cu-Ni(2)@BTC, respectively.

Preparation of the catalytic electrode. 10 mg of Cu-Ni(x)@PA and Nafion D-521 dispersion (20 μL) were added into 1 mL ethanol with to form a homogeneous solution

with the assistance of ultrasound. Then, the mixture was spread onto the CP surface and dried under room temperature to obtain the electrode.

Characterization. Field emission transmission electron microscope (TALOS F200X) was used for the TEM characterizations. TEM samples were prepared by dispersing the sample in ethanol, dropping a droplet of the dispersion onto a copper grid, and then vacuum drying. Scanning electron microscopy (SEM) experiment was carried out with a Hitachi S-4800 SEM operated at 15 kV. SEM samples were prepared by coating the sample on a conductive adhesive. Powder X-ray diffraction (XRD) patterns were collected with a Rigaku D/max-2500 X-ray diffractometer using Cu Kα radiation ($\lambda =$ 0.154 nm). The electrochemical workstation was employed using a CHI 660e (Shanghai CH Instruments Co., China). Fourier transform infrared spectra (FT-IR) were conducted using a Nicolet 6700, within the frequency range of 400~4000 cm^{-1}, using the KBr pellet technique. X-ray photoelectron spectroscopy (XPS, ESCALAB 220i-XLspectrometer) was used to study the element of Cu-Ni(x)@PA hybrids. N_2 adsorption-desorption isotherm were measured at 77K on an Autosorb-iQA3200-4 sorption analyzer (Quantatech Co., USA) instrument. Before measurement, samples were degassed in a vacuum at 150 °C for 3 h. Brunauer-Emmett-Teller (BET) method and Barrett-Joyner-Halenda (BJH) method were employed to calculate the specific surface area and pore size distributions, respectively.

Cyclic voltammetry (CV) measurement. The electrochemical testing was carried out using an electrochemical workstation. Cyclic voltammetry (CV) measurement was performed in a H-type cell separated by Nafion-117 membrane with a three-electrode system consisting of working electrode, platinum gauze auxiliary counter electrode, and Ag/AgCl (saturated potassium chloride) reference electrode. Prior to experiments, N_2

was bubbled through the anolyte to remove air. The electrochemical testing results were presented as potential values versus RHE (E vs RHE = E vs Ag/AgCl + 0.0592 × pH + 0.197 V).

Electrolysis of HMF and product analysis. The electrochemical oxidation of HMF was carried out at room temperature in a typical H-type cell. 1.0 M KOH aqueous solution were used as cathodic and anodic electrolytes, respectively. The amount of electrolyte was 12 mL in all the experiments. Prior to electrolysis, N_2 was bubbled through the anolyte for 30 min to remove air. The product of electrochemical experiments was analyzed by HPLC (Waters E2695) equipped with an ultraviolet detector and C18 column. The detection wavelength was recorded at 280 nm. The column temperature was 35 ºC. The mobile phase consists of $V(H_2SO_4, 0.5 M):V(CH_3OH) = 70:30$ with a flow rate of 0.8 mL/min. The conversion and faradaic efficiency were calculated by HPLC analysis.

$$Faradaic\ efficiency = \frac{Molar\ amount\ of\ product \times\ n \times\ F}{Q} \times 100\%$$

Where n is the transfer electron number, *F* is the faraday constant, and *Q* represents the total charge. For HMFCA, *n* is 2, while for FDCA, n is 6.

Electronic density distribution calculations. Electronic density distribution calculations were carried out by the Gaussian 16 program.[1] M06-2x exchange-correlation functional and LANL2DZ basis set were employed to optimize the initial structures and perform frequency analysis. A simplified model consisting of 1 PA molecule, 1 Ni atom, and 2 Cu atoms was selected. For comparison, a simplified model consisting of 1 PA molecule and 1 Ni atom was also employed. Structures were first

relaxed and equilibrated. The configuration was optimized to be energetically stable, which were confirmed by frequency analysis. After structure optimization, single point calculations are performed to obtain the molecular electrostatic potential followed by a full NBO analysis. [2]

2. Supplementary figures and tables
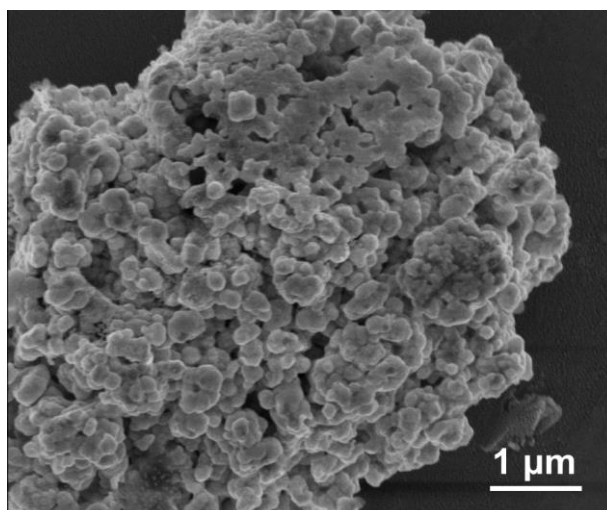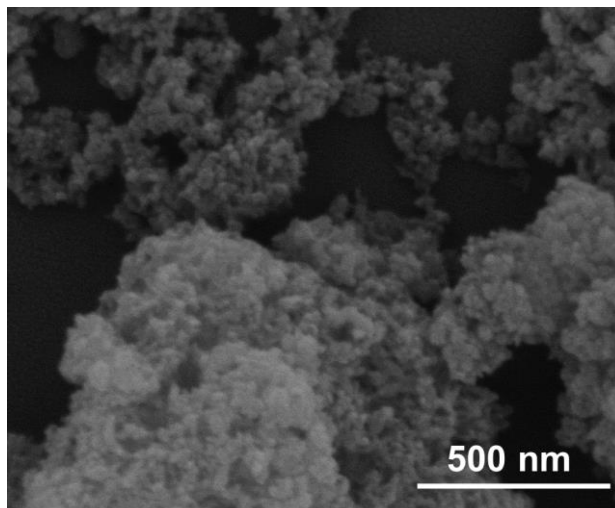

Fig. S1. SEM image of Cu-Ni(1)@ PA

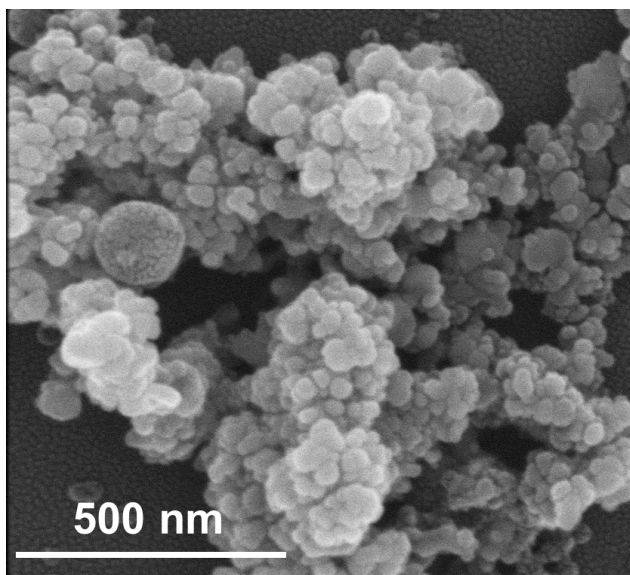Fig. S2. SEM image of Cu-Ni(0.5)@PA

Fig. S3. SEM image of Cu@PA
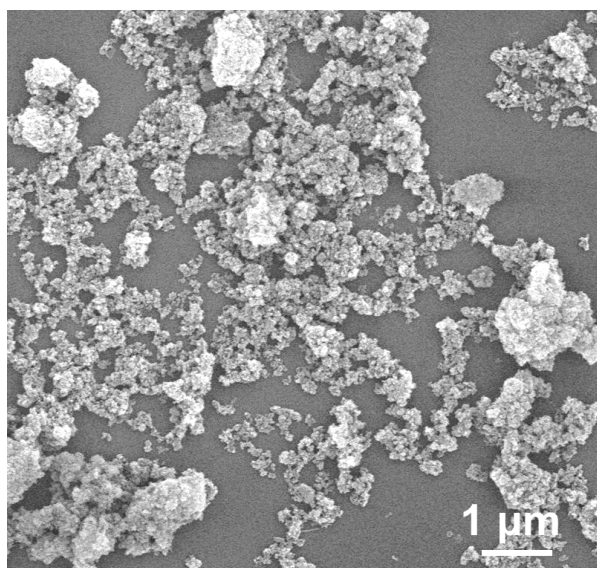
Fig. S4. SEM image of Ni@PA
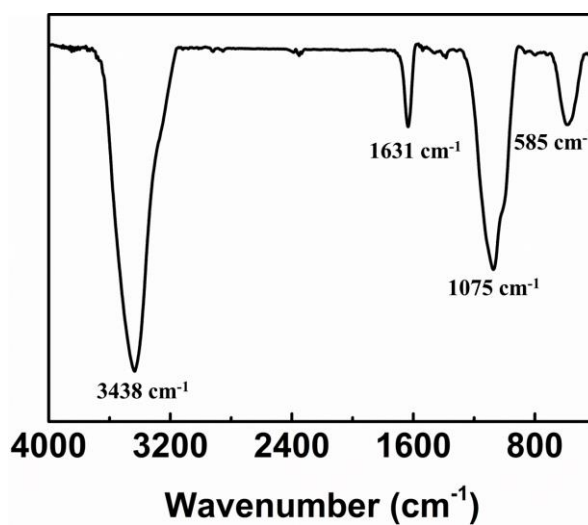
Fig. S5. FT-IR spectrum of Cu-Ni(0.5)@PA

As shown in Fig. S5, the strong absorption at 3438 cm^{-1} is attributed to hydroxyl stretching vibrations. The strong absorptions at 1075 cm^{-1} and 1631 cm^{-1} belong to the phosphate group and phosphate hydrogen group in phytate.[3] The peak at 585 cm^{-1} corresponds to the linkage between metal and oxygen in PA.[4]
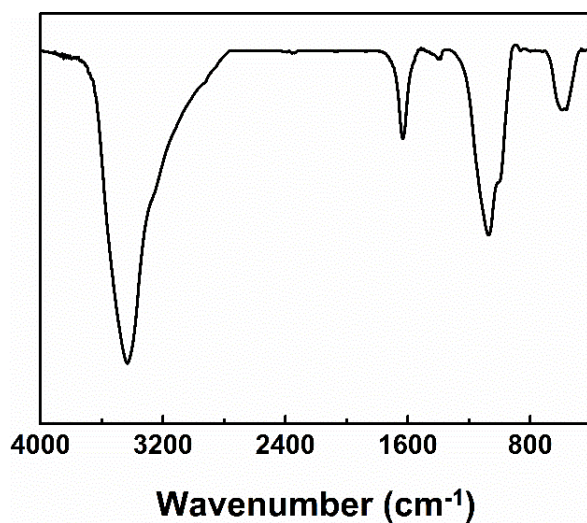
Fig. S6. FT-IR spectrum of Cu-Ni(2)@PA (The FT-IR absorption of Cu-Ni(2)@PA is similar to that of Cu-Ni(0.5)@PA.)
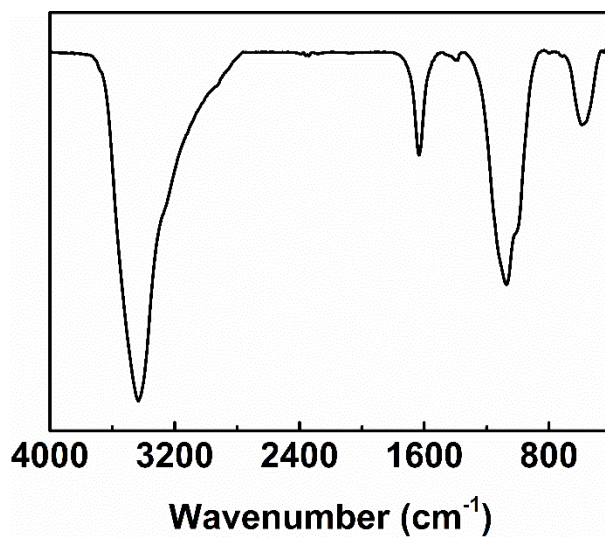
Fig. S7. FT-IR spectrum of Cu-Ni(1)@PA (The FT-IR absorption of Cu-Ni(1)@PA is similar to that of Cu-Ni(0.5)@PA.)
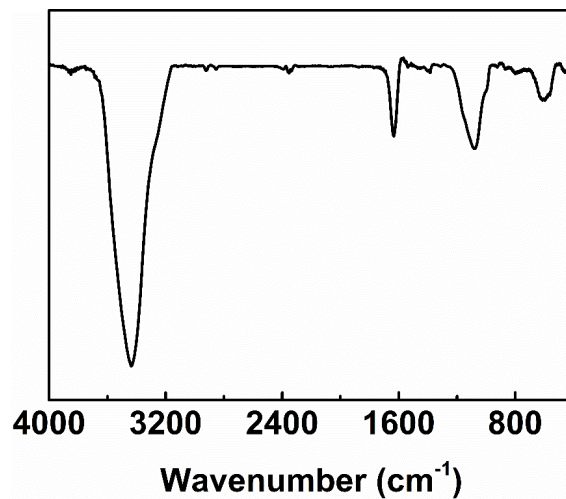
Fig. S8. FT-IR spectrum of Cu@PA (The FT-IR absorption of Cu@PA is similar to that of Cu-Ni(0.5)@PA.)
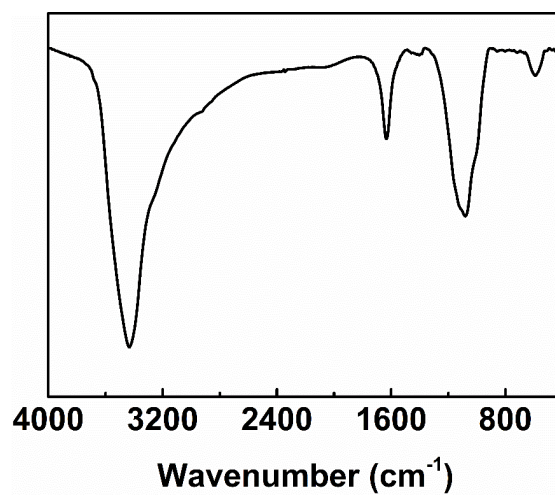
Fig. S9. FT-IR spectrum of Ni@PA (The FT-IR absorption of Ni@PA is similar to that of Cu-Ni(0.5)@PA.)
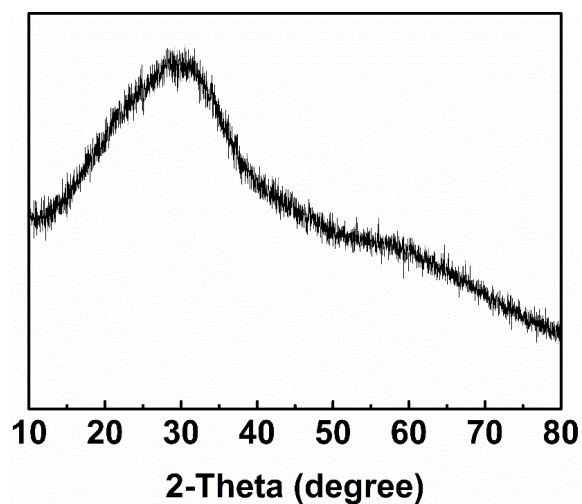
Fig. S10. XRD pattern of Cu-Ni(0.5)@PA

From Fig. S10, the XRD pattern of Cu-Ni(0.5)@PA shows broad diffraction peaks, indicating that Cu-Ni(0.5)@PA has low crystallinity or is poorly ordered, which could be attributed to the irregular connectivity between metal and PA.[5,6]
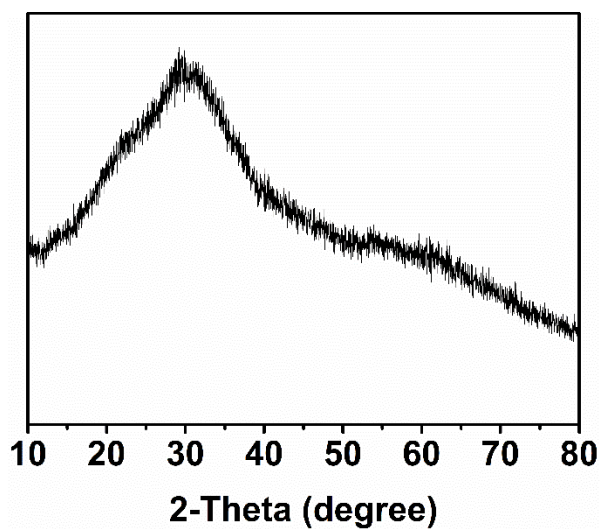
Fig. S11. XRD pattern of Cu-Ni(2)@PA (The XRD pattern of Cu-Ni(2)@PA is similar to that of Cu-Ni(0.5)@PA.)
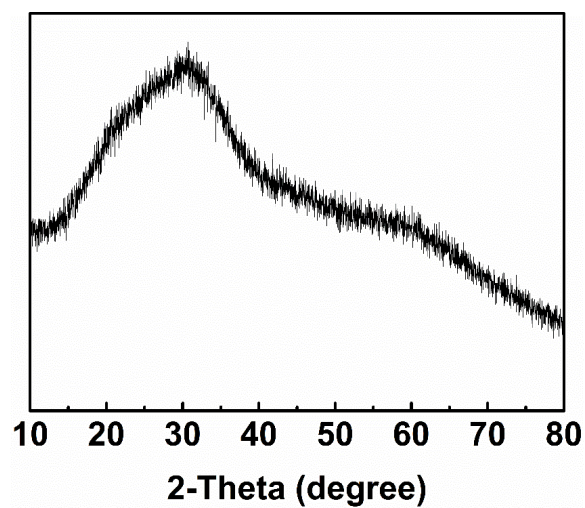
Fig. S12. XRD pattern of Cu-Ni(1)@PA (The XRD pattern of Cu-Ni(1)@PA is similar to that of Cu-Ni(0.5)@PA.)
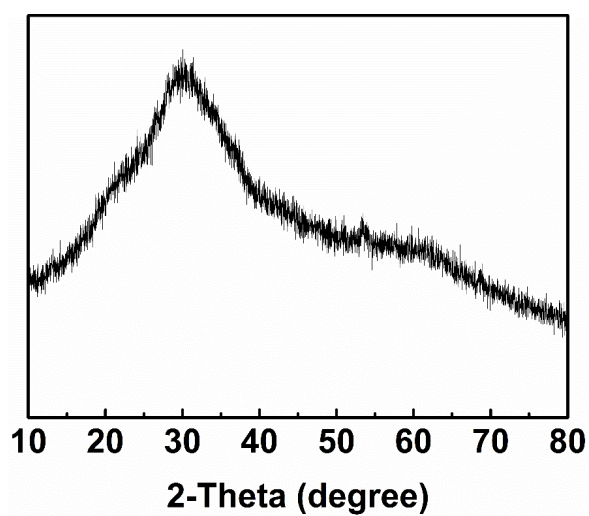
Fig. S13. XRD pattern of Cu@PA (The XRD pattern of Cu@PA is similar to that of Cu-Ni(0.5)@PA.)
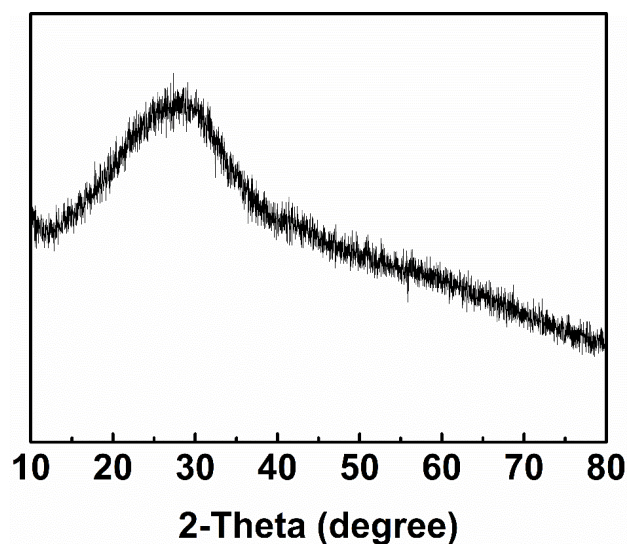
Fig. S14. XRD pattern of Ni@PA (The XRD pattern of Ni@PA is similar to that of Cu-Ni(0.5)@PA.)
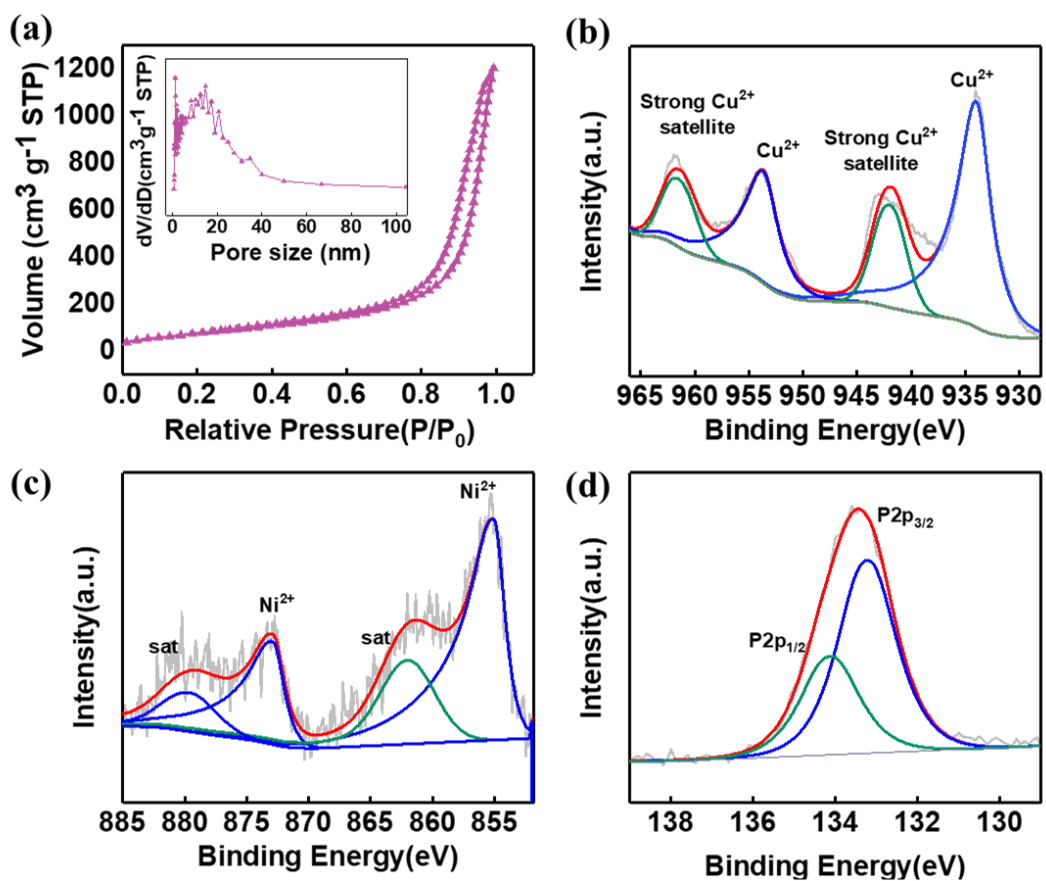
Fig. S15. Characterization of Cu-Ni(2)@PA. (a) N_2 adsorption-desorption isotherms. High-resolution XPS spectra of Cu 2p (b), Ni 2p (c), and P 2p (d).
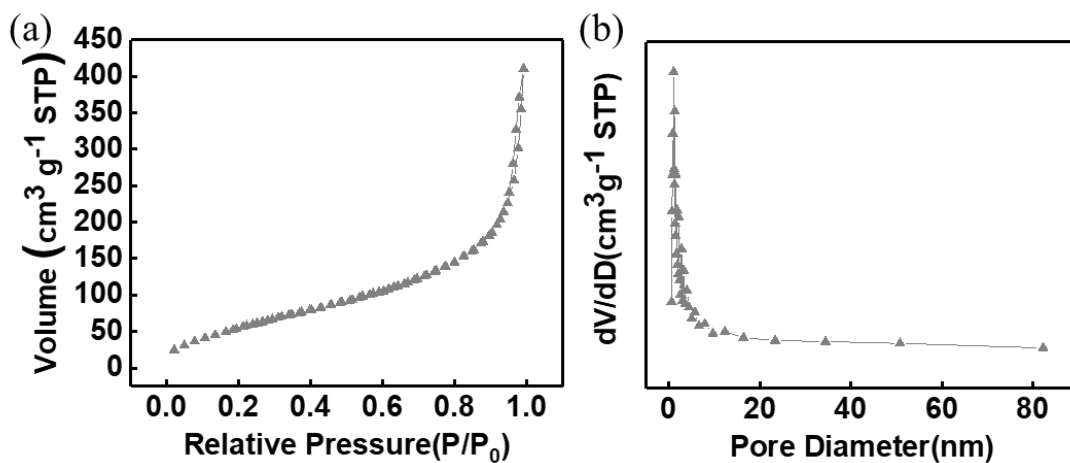
Fig. S16. N$_2$ adsorption-desorption curve of Cu-Ni(0.5)@PA (a) and the corresponding

pore size distribution curve (b).
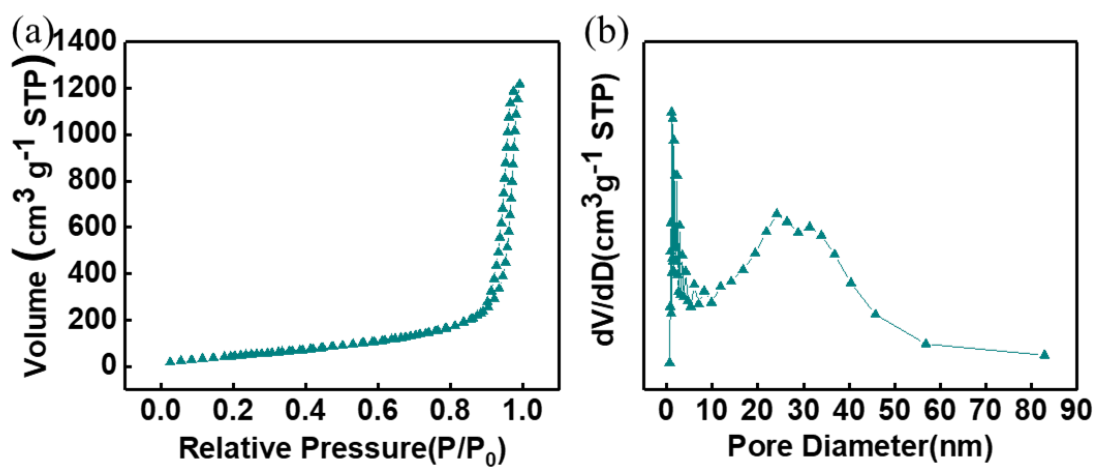
Fig. S17. N$_2$ adsorption-desorption curves of Cu-Ni(1)@PA (a) and the corresponding

pore size distribution curve (b)
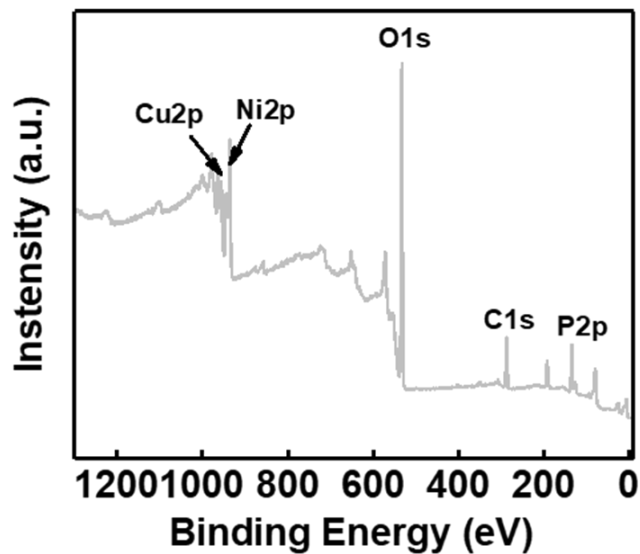
Fig. S18. XPS survey of Cu-Ni(2)@PA

From Fig. S18, it can be observed that the Cu, Ni, C, P, and O elements can be detected, indicating the successful synthesis of Cu-Ni(x)@PA hybrids.
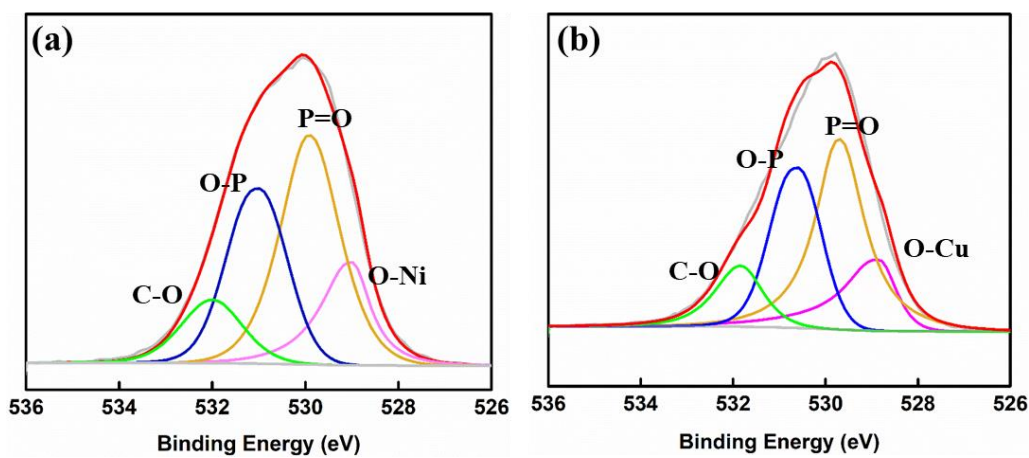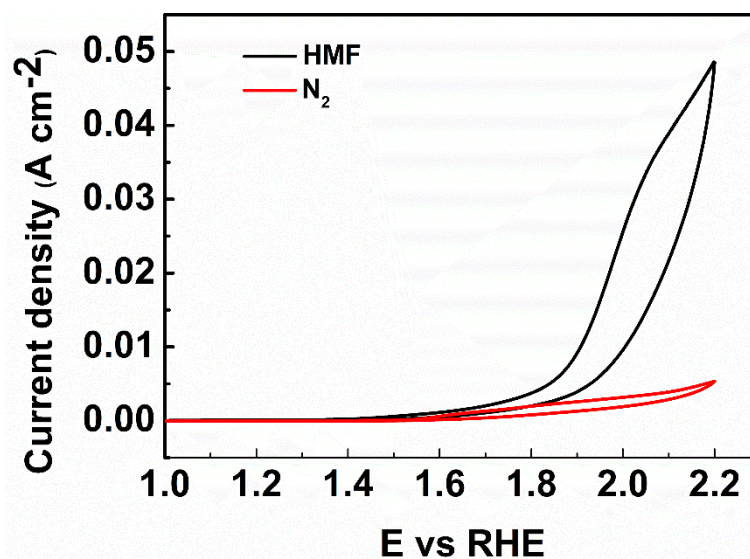

Fig. S19. High-resolution XPS spectra of O 1s in the Ni@PA (a) and Cu@PA (b)

Fig. S20. CV curves of Cu-Ni(2)@PA

As shown in Fig. S20, the current density increased significantly after adding HMF in comparison to N_2, indicating the occurrence of HMF oxidation.
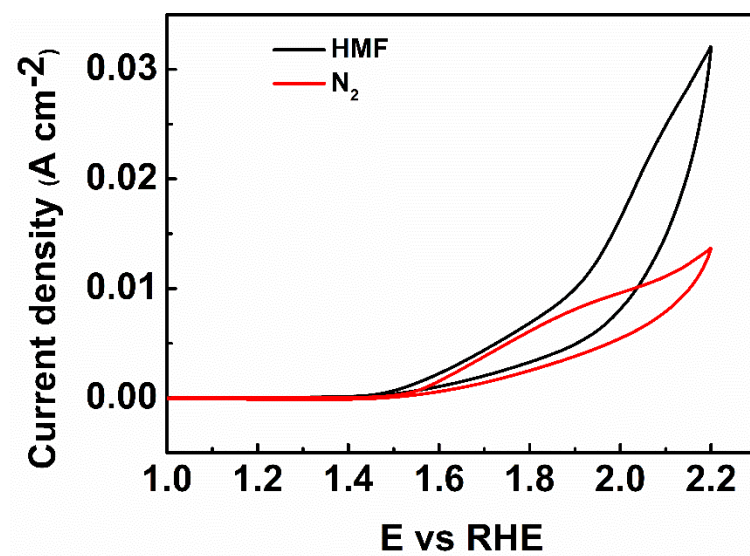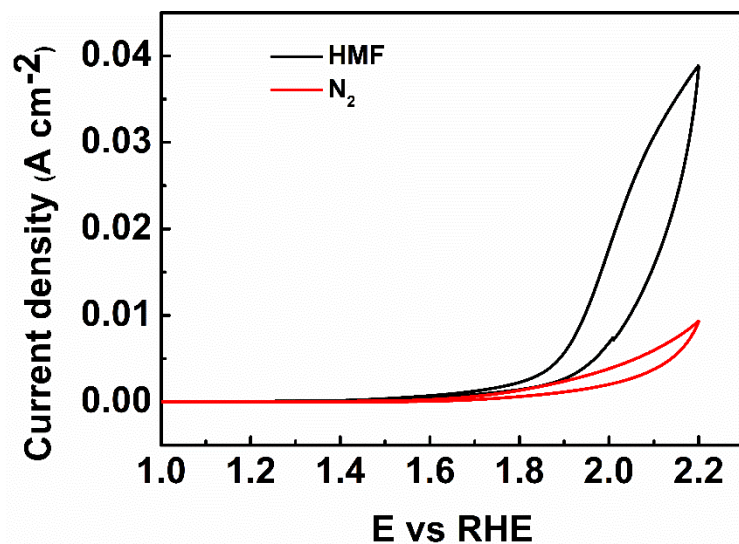

Fig. S21. CV curves of Cu-Ni(0.5)@PA

Fig. S22. CV curves of Cu-Ni(1)@PA

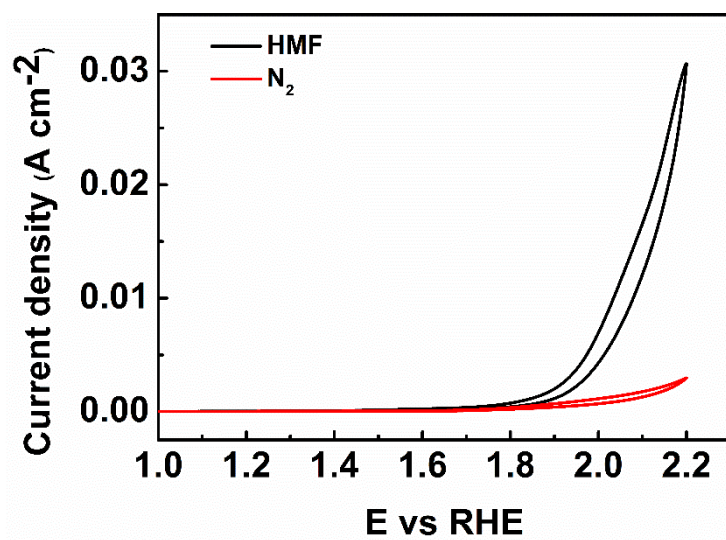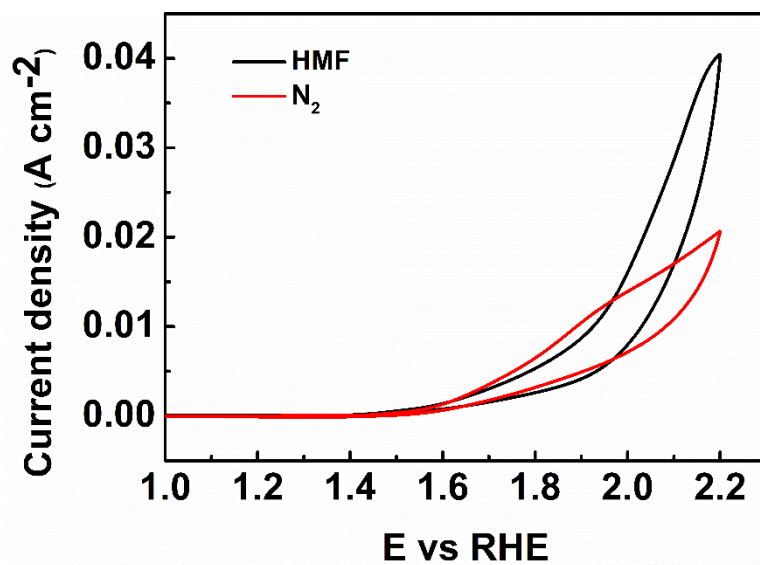

Fig. S23. CV curves of Cu@PA
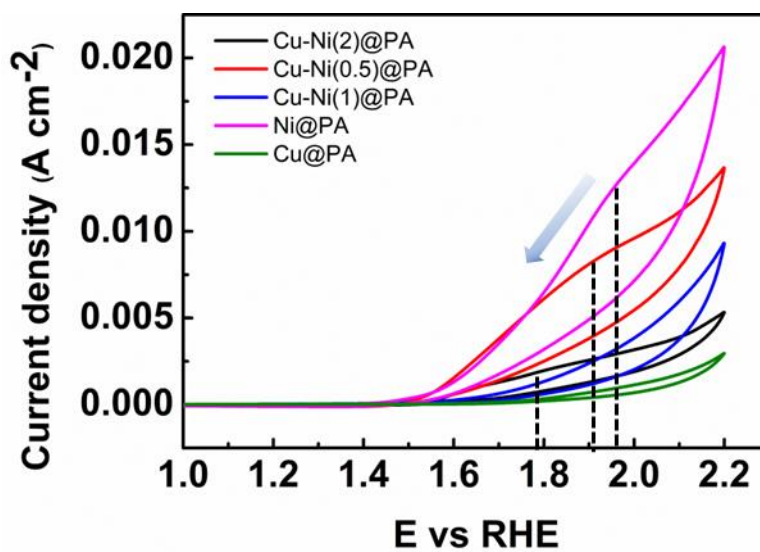
Fig. S24. CV curves of Ni@PA

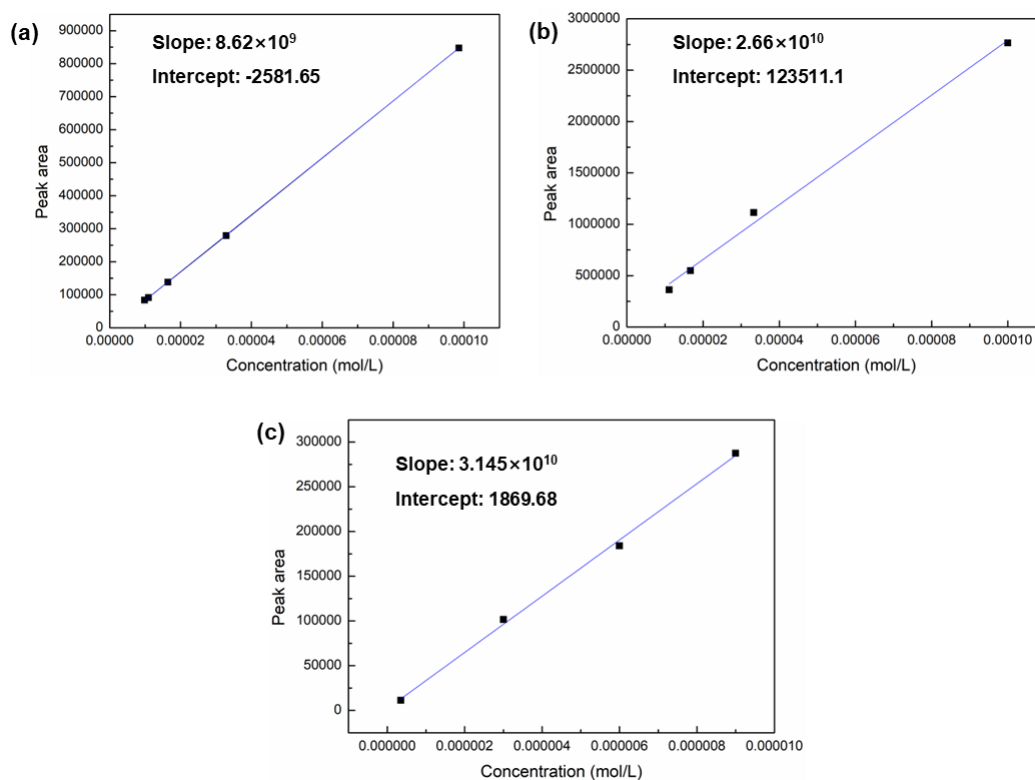Fig. S25. CV curves of Cu-Ni(x)@PA in the presence of N_2

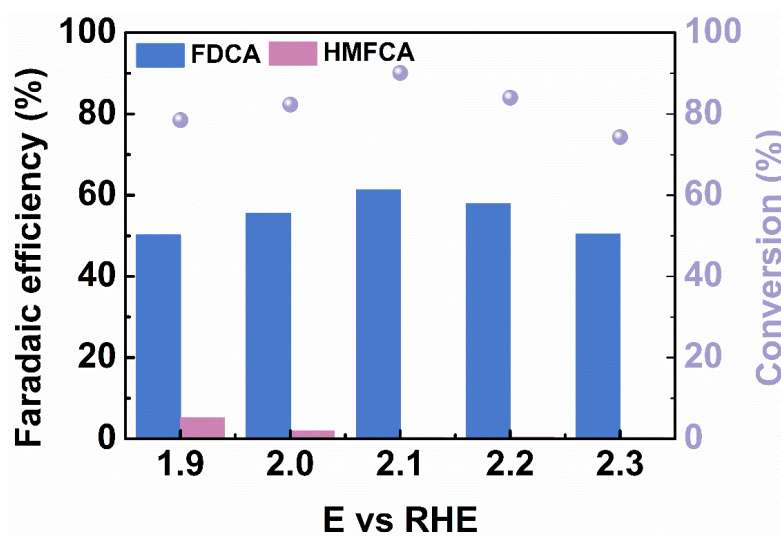Fig. S26. The standard curves of HMF (a), FDCA (b), and HMFCA(c)

Fig. S27. Faradaic efficiency and conversion of HMF oxidation over Cu-Ni(1)@PA at different potentials.
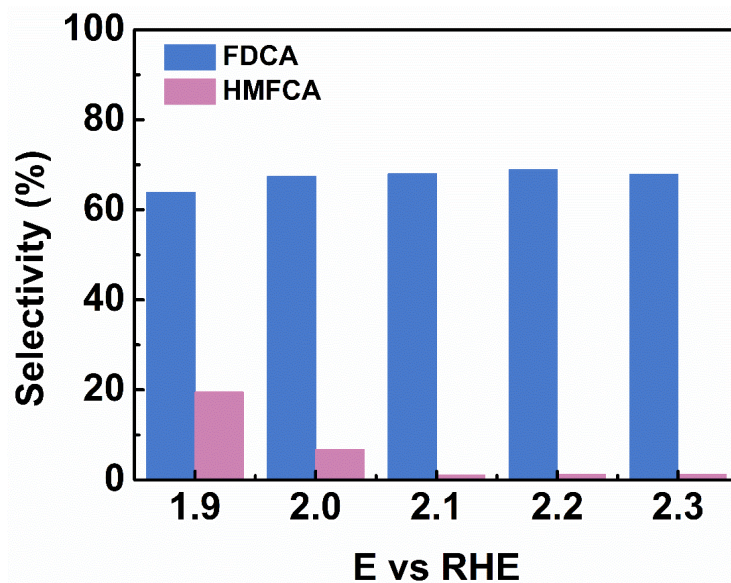
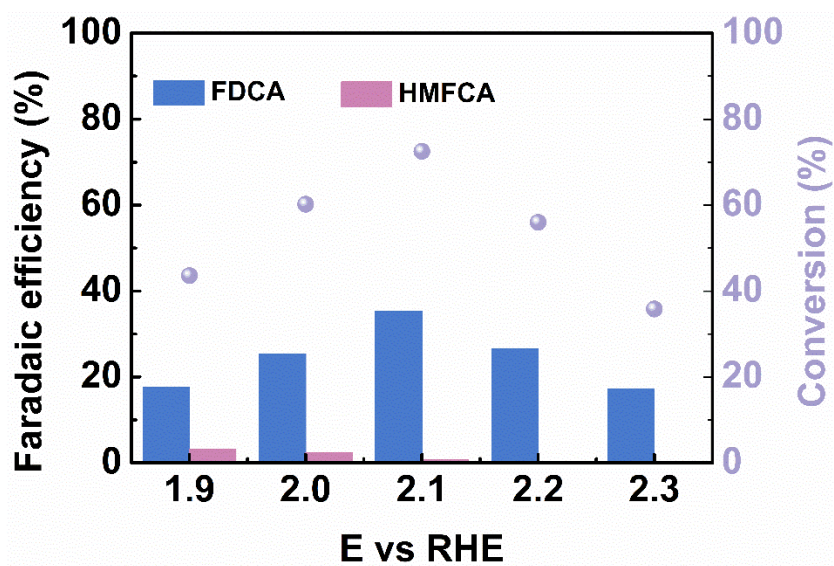Fig. S28. Selectivity of FDCA over Cu-Ni(1)@PA at different potentials.

Fig.S29. Faradaic efficiency and conversion of HMF oxidation over Cu-Ni(0.5)@PA at different potentials.
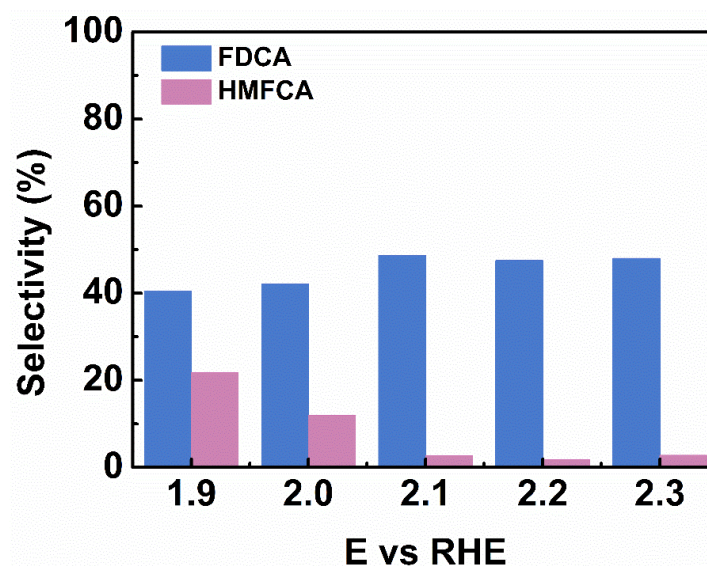
Fig. S30. Selectivity of FDCA over Cu-Ni(0.5)@PA at different potentials.

Fig. S31. Faradaic efficiency and conversion of HMF oxidation over Cu@PA at different potentials.

Fig. S32. Selectivity of FDCA over Cu@PA at different potentials.

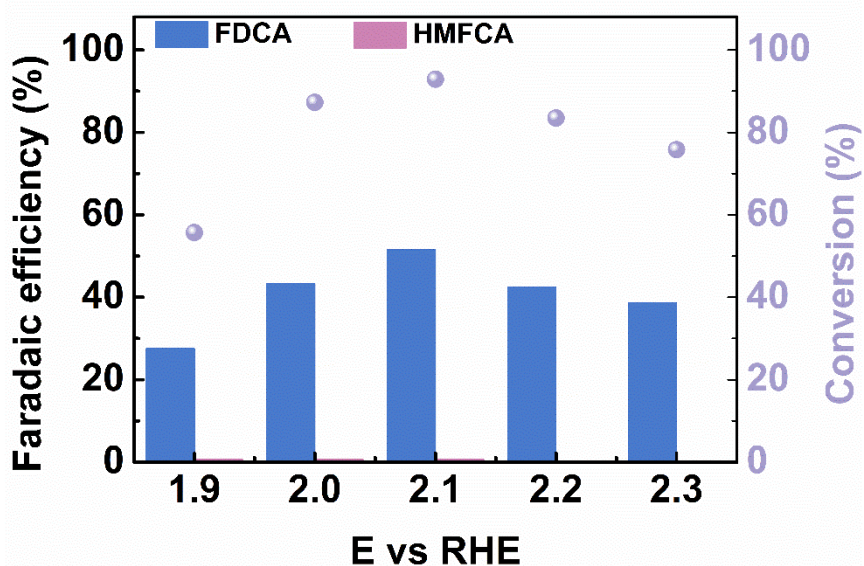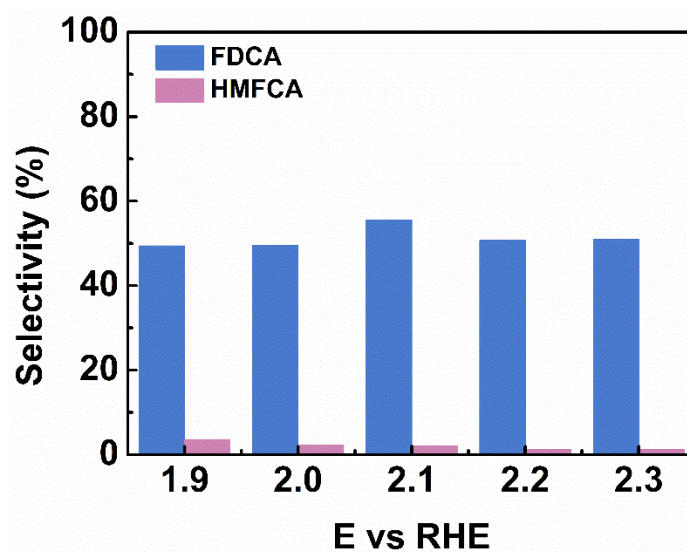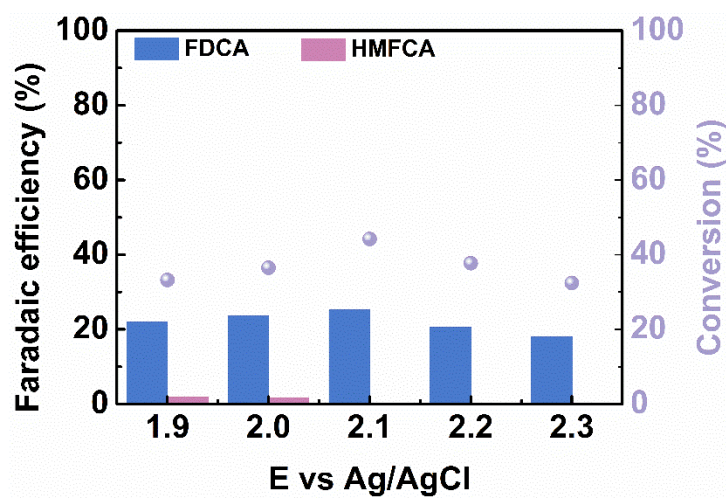Fig. S33. Faradaic efficiency and conversion of HMF oxidation over Ni@PA at different potentials.
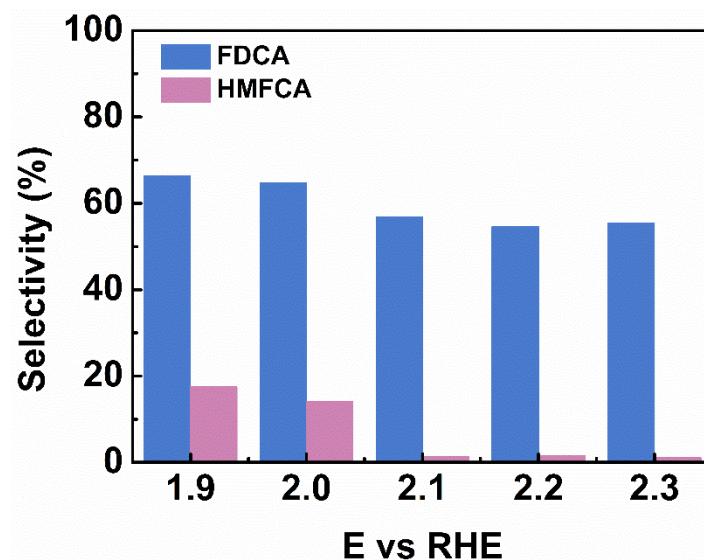
Fig. S34. Selectivity of FDCA over Ni@PA at different potentials.
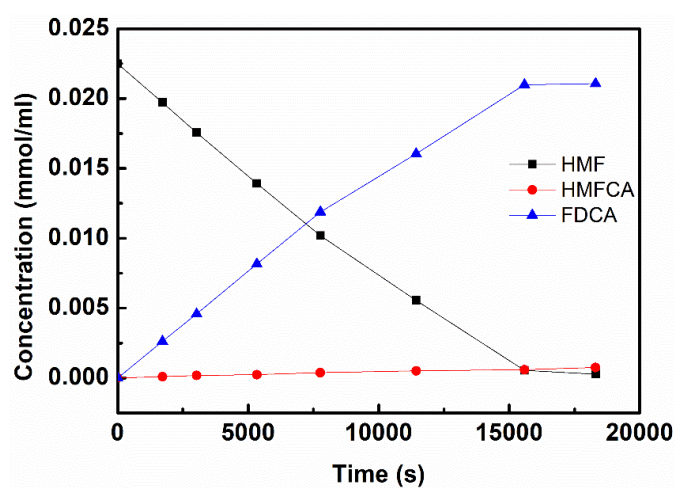
Fig. S35. The change of HMF, HMFCA, and FDCA concentrations over the electrolysis time
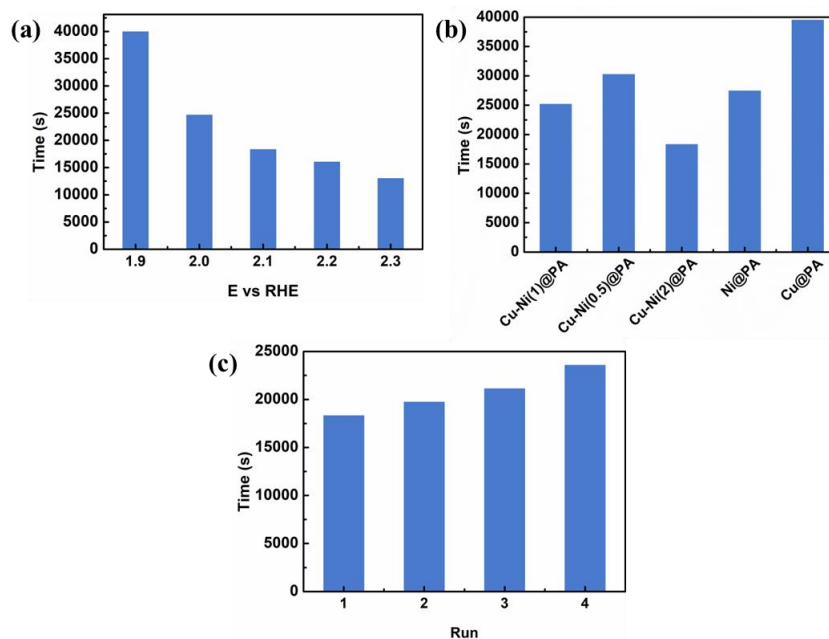
Fig. S36. The reaction time of constant potential polarization. (a) Cu-Ni(2)@PA at different potentials. (b) Different Cu-Ni(x)@PA catalysts at 2.1 V RHE. (c) Cycling performance of Cu-Ni(2)@PA at 2.1 V RHE
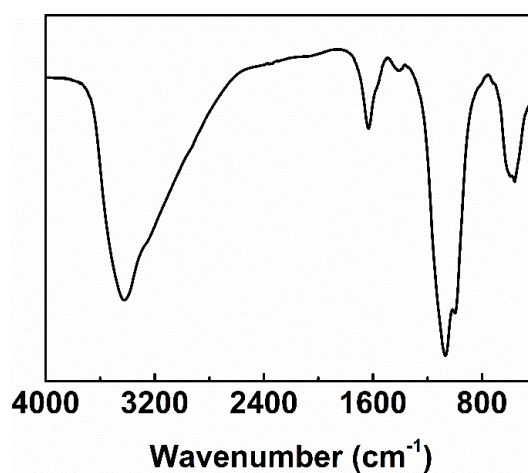
Fig. S37. FT-IR spectrum of the used Cu-Ni(2)@PA after catalytic cycles

From Fig. S37, it can be observed that no obvious difference in the main characteristic peak position of the used Cu-Ni(x)@PA are found after the catalytic cycles, and only the peak intensity at 1000-1150 cm^{-1} increases, indicating the change of connection strength between metal and PA.
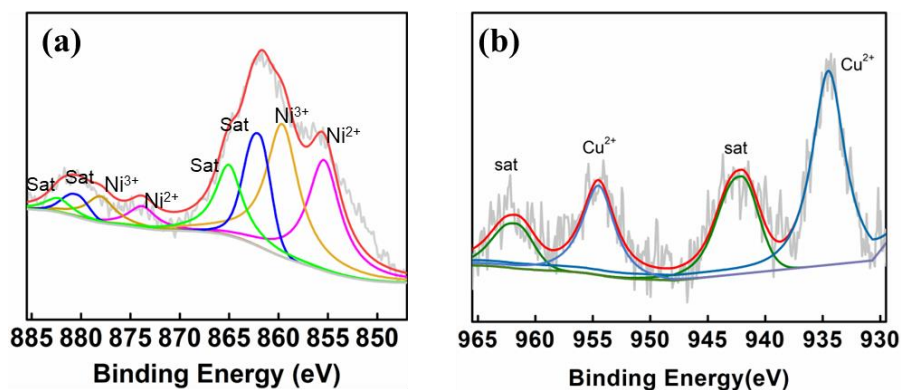
Fig. S38. XPS spectra of Ni 2p (a) and Cu 2p (b) of the used Cu-Ni(2)@PA

Fig. S38 suggests that the Ni^{3+} species are formed after the HMF electrooxidation, suggesting that part of the Ni^{2+} species is converted into the Ni^{3+} species, influencing the connection strength between metal and PA. Combining the reported literature, the Ni^{3+} species also can act as the active species for the HMF oxidation alcohol group,[7] which is helpful to the formation of FDCA. Therefore, the high performance of Cu-Ni(2)@PA for the HMF oxidation can be retained.

Fig. S39. High-resolution XPS spectra Cu 2p of Cu-Ni(2)@PA and Cu@PA.

BTC   ATMP
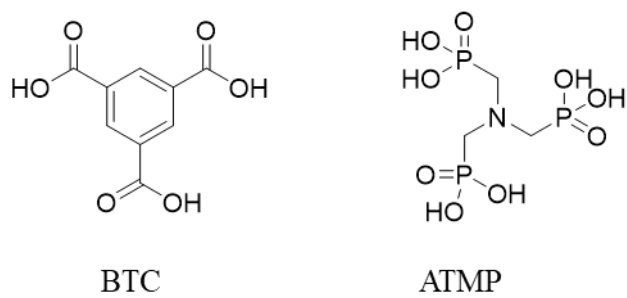
Fig. S40. Molecular structure of BTC and ATMP
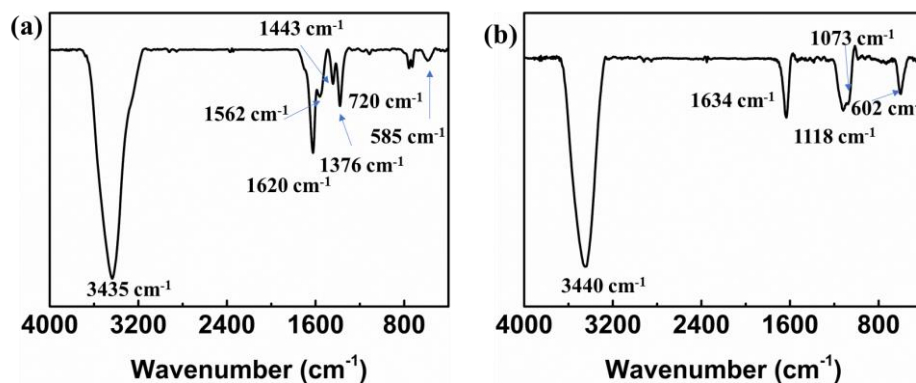
Fig. S41. FT-IR spectra of Cu-Ni(2)@BTC (a) and Cu-Ni(2)@ATMP (b)

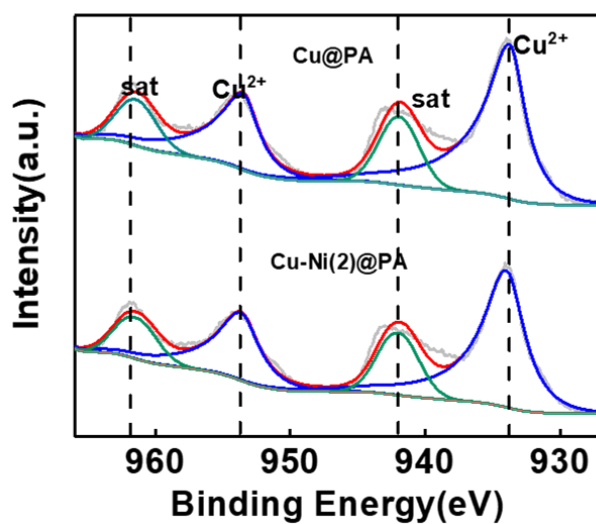As shown in Fig. S41a, the broad band at 3435 cm^{-1} is attributed to stretching vibrations of hydroxyl groups. The strong absorption bands at 1620 cm^{-1}, 1562 cm^{-1}, 1443 cm^{-1}, 1376 cm^{-1} are ascribed to asymmetric, and symmetric carboxylate groups existed in BTC, while the peak at 720 cm^{-1} is assigned to C–H out-of-plane bending vibration.[8] The peak at 585 cm^{-1} belongs to the linkage between metal and oxygen in BTC.[9] From Fig. S41b, the peaks at 1073 cm^{-1}, 1118 cm^{-1} and 1634 cm^{-1} are attributed to the phosphate and phosphate hydrogen groups.[10,11] The peak at 602 cm^{-1} belongs to the linkage between metal and oxygen in ATMP. [3]

Fig. S42. Effect of different ligands on the HMF oxidation. (a) CV curves in the presence of HMF. (b) Performance comparison. (c) Tafel plots. (d) EIS spectra.

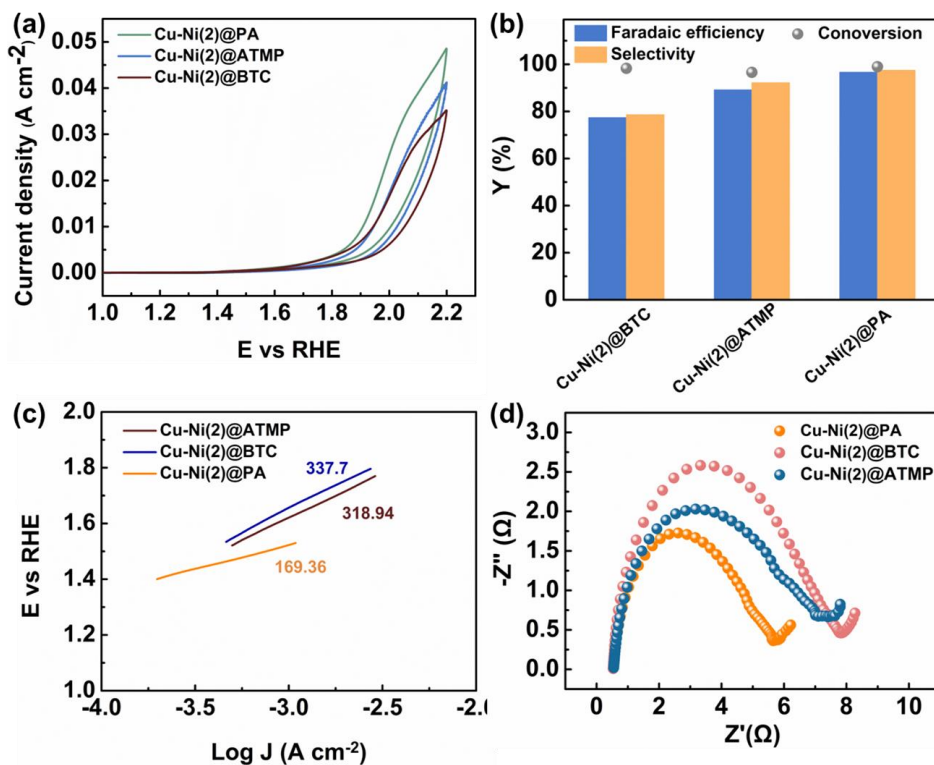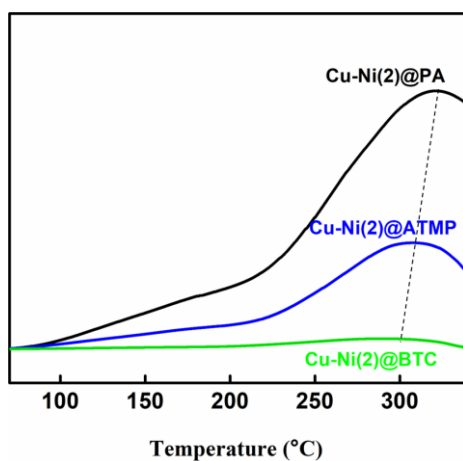Fig. S43. The ammonia temperature-programmed desorption results of Cu-Ni(2)@PA, Cu-Ni(2)@ATMP, and Cu-Ni(2)@BTC
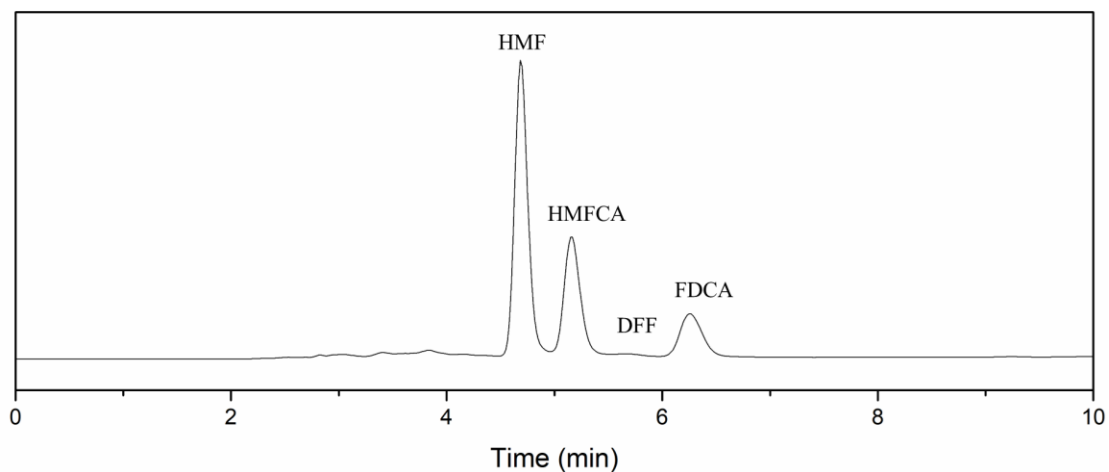
Fig. S44. HPLC chromatograms of the electrochemical oxidation of HMF over Cu-Ni(2)@PA

Table S1. Porosity properties of Cu-Ni(x)@PA with different Cu-Ni mole ratios

Sample	Surface area [a] $(m^2\ g^{-1})$	Pore volume [b] $(cm^3\ g^{-1})$	Pore size [c] (nm)
Cu-Ni(0.5)@ PA	211.6	1.89	17.9
Cu-Ni(1)@ PA	225.9	0.64	5.7
Cu-Ni(2)@ PA	293.3	1.87	12.7

[a] Surface area was calculated by the Brunauer–Emmett–Teller (BET) method.

[b] Total pore volume was obtained using the adsorption branch of the N_2 isotherm at P/P_0 = 0.99.

[c] Average pore diameter was determined from the local maximum of the BJH distribution of pore diameters obtained in the adsorption branch of the N_2 isotherm.

Table S2. Porosity properties of the control samples

Sample	Surface area [a]	Pore volume [b]	Pore size [c]
	$(m^2\ g^{-1})$	$(cm^3\ g^{-1})$	(nm)
Cu-Ni(2)@PA	293.3	1.87	12.7
Cu-Ni(2)@ATMP	86.8	0.67	15.3
Cu-Ni(2)@BTC	81.1	0.31	7.67

[a] Surface area was calculated by the Brunauer–Emmett–Teller (BET) method.

[b] Total pore volume was obtained using the adsorption branch of the N_2 isotherm at P/P_0 = 0.99.

[c] Average pore diameter was determined from the local maximum of the BJH distribution of pore diameters obtained in the adsorption branch of the N_2 isotherm.

Notes and references

1. M. J. Frisch, G. W. Trucks, H. B. Schlegel, G. E. Scuseria, M. A. Robb, J. R. Cheeseman, G. Scalmani, V. Barone, B. Mennucci, G. A. Petersson, H. Nakatsuji, M. Caricato, X. Li, H. P. Hratchian, A. F. Izmaylov, J. Bloino, G. Zheng, J. L. Sonnenberg, M. Hada, M. Ehara, K. Toyota, R. Fukuda, J. Hasegawa, M. Ishida, T. Nakajima, Y. Honda, O. Kitao, H. Nakai, T. Vreven, J. A. J. Montgomery, J. E. Peralta, F. Ogliaro, M. Bearpark, J. J. Heyd, E. Brothers, K. N. Kudin, V. N. Staroverov, R. Kobayashi, J. Normand, K. Raghavachari, A. Rendell, J. C. Burant, S. S. Iyengar, J. Tomasi, M. Cossi, N. Rega, N. J. Millam, M. Klene, J. E. Knox, J. B. Cross, V. Bakken, C. Adamo, J. Jaramillo, R. Gomperts, R. E. Stratmann, O. Yazyev, A. J. Austin, R. Cammi, C. Pomelli, J. W. Ochterski, R. L. Martin, K. Morokuma, V. G. Zakrzewski, G. A. Voth, P. Salvador, J. J. Dannenberg, S. Dapprich, A. D. Daniels, O. Farkas, J. B. Foresman, J. V. Ortiz, J. Cioslowski and D. J. Fox, Gaussian 16, Revision A.03. Gaussian Inc., Wallingford, CT, 2016.

2. S. Liu and L. G. Pedersen, *J. Phys. Chem. A*, 2009, 113, 3648-3655.

3. H. Wu, J. Song, C. Xie, Y. Hu, J. Ma, Q. Qian and B. Han, *Green Chem*., 2018, 20, 4602-4606.

4. R. Yan, X. Gao, W. He, R. Guo, R. Wu, Z. Zhao and H. Ma, *RSC Adv*., 2017, 7, 41152-41162.

5. X. Song, Y. Chen, M. Rong, Z. Xie, T. Zhao, Y. Wang, X. Chen and O. S. Wolfbeis, *Angew. Chem. Int. Ed*., 2016, 55, 3936-3941.

6. J. Song, B. Zhou, H. Zhou, L. Wu, Q. Meng, Z. Liu and B. Han, *Angew. Chem. Int. Ed*., 2015, 54, 9399-9403.

7. J. Woo, B. C. Moon, U. Lee, H.-S. Oh, K. H. Chae, Y. Jun, B. K. Min and D. K. Lee,

ACS Catal., 2022, 12, 4078-4091.

8. Z. Li, N. Hori and A. Takemura. *Cellulose*, 2020, 27, 1733-1744.

9. H. Ghafuri, F. Ganjali and P. Hanifehnejad. *Chem. Proc*., 2021, 3, 2.

10. G. A. Bhat and R. Murugavel, *J. Mol. Struct*., 2021, 1224, 128960.

11. X. Li, G. Ding, B. L. Thompson, L. Hao, D. A. Deming, Z. M. Heiden and Q. Zhang, *ACS Appl. Mater. Interfaces*, 2020, 12, 30670-30679.